ACS APPLIED MATERIALS & INTERFACES

www.acsami.org

Research Article

Plasmofluidic-Based Near-Field Optical Trapping of Dielectric Nano-Objects Using Gold Nanoislands Sensor Chips

Guangyu Qiu,[▽] Ying Du,[▽] Yujia Guo, Yingchao Meng, Zhibo Gai, Ming Zhang, Jing Wang,* and Andrew deMello*

Cite This: *ACS Appl. Mater. Interfaces* 2022, 14, 47409−47419

Read Online

ACCESS | Metrics & More | Article Recommendations | Supporting Information

ABSTRACT: Near-field optical manipulation has been widely used for guiding and trapping nanoscale objects close to an optical-active interface. This near-field manipulation opens opportunities for next-generation biosensing with the capability of large-area trapping and in situ detection. In this article, we used the finite element method (FEM) to analyze the motion mechanism of nano-objects (50−500 nm) in the near-field optics, especially localized surface plasmon resonance (LSPR). The size-dependent optical forces and hydrodynamic forces of subwavelength nanoparticles (<500 nm) in different hydrodynamic velocity fields were calculated. When the strength of the local electric field was increased, LSPR with two-dimensional gold nanoislands (AuNIs) showed improved capability for manipulating nano-objects near the vicinity of the AuNI interface. Through the experiments of *in situ* interferometric testing 50−500 nm nano-objects with constant number concentration or volume fraction, it was confirmed that the local plasmonic near-field was able to trap the dielectric polystyrene beads smaller than 200 nm. The plasmofluidic system was further verified by testing biological nanovesicles such as exosomes (40−200 nm) and high- and low-density lipoproteins (10−200 nm). This concept of direct dielectric nano-objects manipulation enables large-scale parallel trapping and dynamic sensing of biological nanovesicles without the need of molecular binding tethers or labeling.

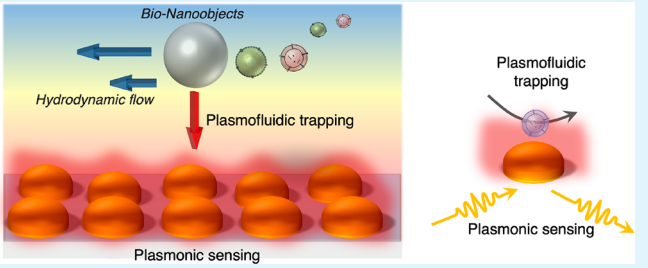

KEYWORDS: *evanescent field, plasmonic trapping, optofluidic, finite element method, biosensing, microfluidic device*

INTRODUCTION

The manipulation of nano-objects has attracted widespread attention in many promising multidisciplinary fields such as nanomedicines, biomolecular characterization, and selective nanocatalysis.[1−4] The key to achieve micro- and nano-manipulation is to control the motion of nano-objects by using suitable external fields, such as electric, magnetic, optic, and acoustic fields.[5−8] Conventional optical trapping techniques based on the focused laser beam requires a bulky equipment and expensive high numerical aperture lens. Moreover, the trapping field generated by the focused laser has difficulties in manipulating particles with dimensions of tens of nanometers.[1] On the one hand, the interaction force between light and the particle becomes remarkably weak in the nanoscale range, particularly for optical trapping described by ray optics and without considering the polarization of the particle and Lorentz force. Objects in optical manipulation with a focused light beam usually have the size comparable to the wavelength (i.e., $0.5 \times \lambda$ to $20 \times \lambda$).[9] On the other hand, the thermal motion of the nanometric objects is enhanced due to the reduction of viscous drag.[10]

The novel domain of near-field optics refers to the coupling effect of light to form a subwavelength feature, and comes to the forefront due to the prospect of overcoming the diffraction limit.[11,12] The manipulation with near-field optics permits new possibilities for large-area deflecting and trapping of micro- and nano-objects.[13,14] It has been demonstrated that optical forces arising from total internal reflection (TIR) excited evanescent wave, such as the waveguides and optical resonators, can be strong enough to hold a single nanoparticle at the dielectric interface.[15] When a two-dimensional plasmonic nanofilm is employed and the optical wave satisfies the surface plasmon polaritons (SPP) excitation condition, a dramatic near-field intensity enhancement appears in the immediate vicinity of the metal-dielectric interface. Due to the associated field enhancement, the SPP mode is used to order and trap colloidal aggregations.[16,17] Generally, the penetration depth of the plasmonic field (i.e., the spatial length of the evanescent decay in the dielectric medium) is about several hundred nanometers (comparable to the excitation wavelength) when using visible light excitation. Localized surface plasmon resonance (LSPR)

Received: July 15, 2022
Accepted: October 7, 2022
Published: October 14, 2022

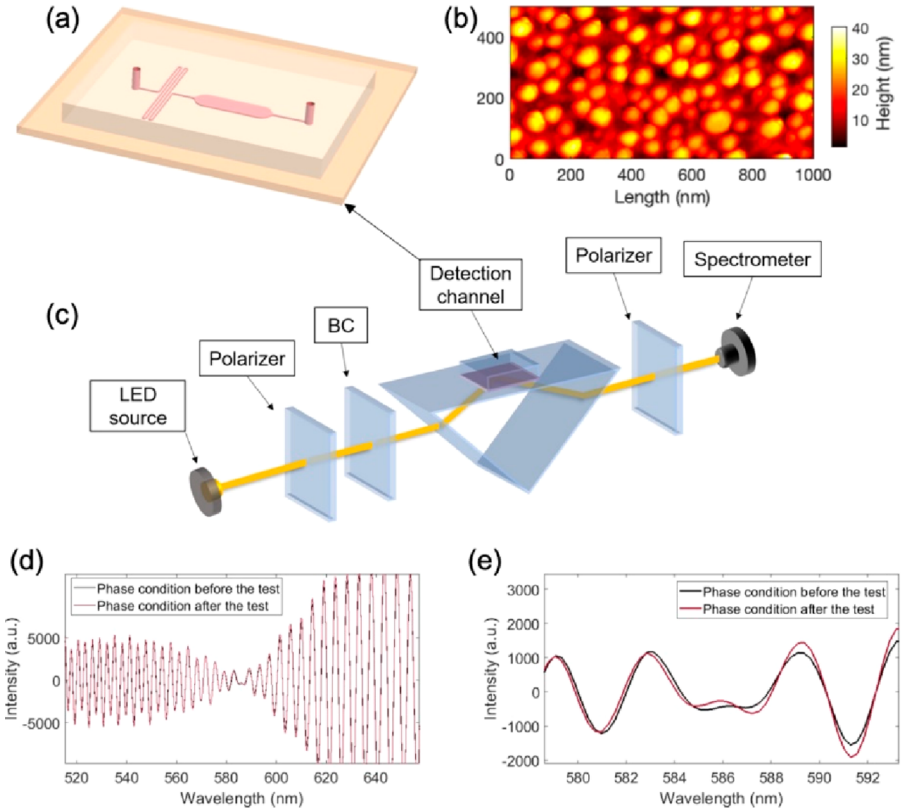

Figure 1. Optical configuration of the plasmofluidic system. (a) The microfluidic chip consisted of a low-profile chamber with dimensions of 10 mm in length, 2 mm in width and 0.1 mm in height. (b) The AFM morphology of the two-dimensional distributed AuNIs. (c) The schematic CPSI setup for the plasmofluidic tests. (d) The full interferometric spectra and (e) the enlarged LSPR response region demonstrated the phase difference of the plasmofluidic test. The plasmonic response toward the nanoparticle trapping or deflection was calculated based on the differential phase between the two spectra.

is a strong localized electromagnetic near-field effect associated with an array of plasmonic nanostructures.[18] The LSPR effect exhibits an extremely tight confinement of free electrons near the vicinity of the nanostructures, and the induced field enhancement is orders of magnitude stronger than the incident beam.[19] Therefore, compared with the nature of evanescent wave and SPP mode, the LSPR near-field creates a highly intensive and localized trapping potential close to the interface, thus providing facile routes for extending the optical trapping to the nanoscale and allowing the plasmonic field to selectively trap particles of different sizes.[17,20] The LSPR near-fields, exited in designed nanostructures, have been proven to be able to trap a single nanoparticle down to less than 10 nm.[21−26] Furthermore, the plasmofluidics which combine the high-aspect-ratio (with low profile height) microfluidic channels and the plasmonic near-field has become an efficient and easy-to-implement platform for bioanalytical and molecular biology studies.[27] With large-scale fabrication of trapping arrays based on designed nanostructures, the next-generation sensors could enable massive parallel trapping and dynamics sensing of nanoscale biomarkers without molecular tethers or labeling.[17,28,29] The plasmofluidic system could perform combinational tasks such as optical trapping, rapid preconcentration, and label-free detection, thus creating a new set of nanoplasmonic sensing metrics.[30] Since the microfluidic field and the plasmonic trapping field coexist in the plasmofluidic system, it is of great significance to have a better understanding of the mechanism of dynamic trapping, deflection and manipulation.

In this work, we experimentally and theoretically investigated the near-field plasmonic deflection of nanoscale objects in a microfluidic geometry. We first compared the theoretical electromagnetic fields of three different TIR configurations, namely, (i) evanescent field at the bare dielectric interface, (ii) SPP field on the Au film, and (iii) LSPR field on the gold nanoislands (AuNIs) layer. The comprehensive finite-element method (FEM, COMSOL Multiphysics) simulation of plasmonic induced near-field deflection force, hydrodynamic drag force and stochastic Brownian motions of nano-objects were presented with a model based on the high-aspect-ratio microfluidic system. Meanwhile, the LSPR photonic chips which contained large-scale gold nanoislands (AuNIs) were employed as a plasmonic active interface to perform the *in situ* nano-objects trapping and detection, thus confirming the near-field manipulation of nanoparticles within different hydrodynamic flow conditions. Our near-field trapping analysis provides insights into the dynamic trapping behavior of nano-objects within a plasmofluidic system, which will empower the functionalities of the next-generation plasmofluidics sensors.

MATERIALS AND METHODS

Optical Configuration. The plasmofluidic chip as shown in Figure 1a consisted of a plasmonic AuNIs substrate, and a microfluidic PDMS bonded layer. The tapping mode atomic force microscopy (TM-AFM) was employed to characterize the topography of the AuNIs. It was found that the quasi-spherical AuNIs with a median diameter of 40 nm were closely packed on the substrate and partially embedded into the BK7 glass substrate, as shown in Figure 1b. The thickness of the sputtered gold nanofilms and the heating

https://doi.org/10.1021/acsami.2c12651
ACS Appl. Mater. Interfaces 2022, 14, 47409−47419

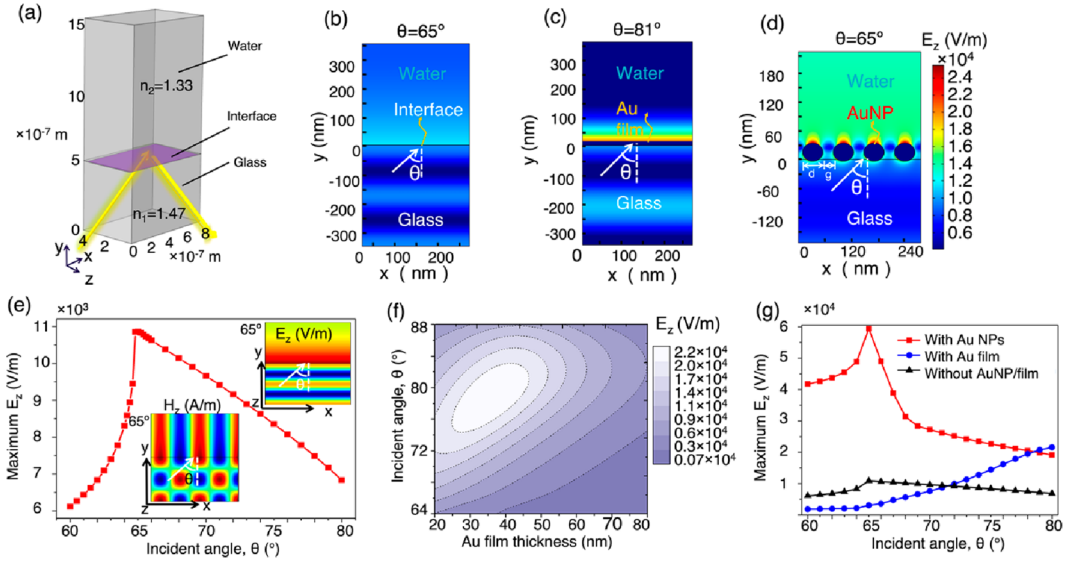

Figure 2. (a) Schematic illustration of the simulation model for local evanescent filed investigation at the glass/water interface. The calculated electric field distributions for (b) glass/water interface, (c) SPP of Au/water interface and (d) LSPR of AuNI/water interface (with 40 nm diameter and 20 nm interparticle gap). (e) Angular distribution of the maximum electric field intensity (Ez) for the glass/water configuration. The insets show the electric and magnetic field distributions. (f) The maximum electric field intensity (Ez) of Au film/glass configuration as a function of the incident angle and Au film thickness. (g) The Ez intensity comparison between different configurations with bared glass, Au film (thickness of 45 nm), and Au nanoparticles (mean diameter of 40 nm). The x direction represented the liquid flow direction and y direction referred to the direction perpendicular to the AuNIs interface.

conditions for AuNI thermal dewetting are the most important parameters in controlling the plasmonic feature of AuNIs and were thus precisely regulated in our experiments, allowing us to produce highly reproducible sensor chips. The optical configuration of the plasmofluidics for *in situ* trapping and detection of nanospheres is shown in Figure 1c. This common-path spectrum interferential (CPSI) sensing system consisted of a broadband LED source (Thorlabs, MWWHD3) with the emission spectrum ranging from 480 to 730 nm. An yttrium vanadate (YVO_4) birefringent crystal (BC) introduced a sufficient optical path difference to create the interferometric patterns as shown in Figure 1d. A BK7 right-angle prism bonded to the plasmofluidic chip was used to fulfill the TIR configuration and excite LSPR near-field. The measured optical power density for LSPR excitation was 1.3 W/m^2. Based on our recent research works on dual-functional thermoplasmonic sensing system, this low incident power density is insufficient to cause a significant temperature elevation.[31] A temperature-stabilized spectrometer (Avantes, AvaSpec-ULS2048) covering 350−840 nm was used to record the common-path spectral interference (CPSI) signal. Spectral interferograms with and without trapped nanoparticles were given in Figure 1d,e. The maximum phase response could be retrieved at the resonance wavelength (i.e., 586 nm).

Theoretical Models for Studying the Nar-Field Trapping and the Hydrodynamic Flow. The plasmonic near-fields and microfluidic hydrodynamic interactions were simulated by FEM based on the commercial software COMSOL (MA, USA). In brief, three different near-field simulations were conducted, including the TIR evanescent field at the glass surface, SPP at the interface with a gold film, and LSPR at the interface with gold nanoparticles. In our LSPR model, AuNIs were simplified to nanospheres with a diameter of 40 nm, and these AuNIs were partially embedded in the glass substrate to a depth of 4 nm.[32] The Wave Optics Module was used to simulate the transmission/reflection spectra and electric/magnetic field profiles for the proposed devices. Based on the experimental condition, the energy density of the incident light was set to 1.3 W/m^2. Due to this low optical power density, we did not consider the effect of thermoplasmonic heating, temperature gradient, and hot Brownian motion in the simulation works. The hydrodynamic fluid was modeled using creeping flow from the Microfluidics Module, which solved for the steady-state fluid dynamics. The Particle Tracing Module offers a particle-based approach to solve the particle trajectory and distribution in the case of purely diffusive motion (Brownian motion) and combined convective motion and diffusive motion. More details of the simulation can be found in the "Methodology" section of the Supporting Information.

Trapping and Detection of Nanospheres with AuNI-Based Plasmofluidic Chip. The deionized water was employed as the reference buffer to build a stable phase reference for the differential phase detection throughout the tests. The trapping targets (i.e., the polystyrene (PS) nanospheres) were suspended in deionized water and, to prevent aggregation, sonicated in an ultrasonic bath for 20 min before the experiment. PS nanospheres have a density of 1.05 g/cm^3 and a refractive index of 1.59 at 589 nm and 25 °C. Compared to other kinds of nano-objects, such as metal nanoparticles, PS nanospheres have properties that more closely match those of the targeted biological nanovesicles. The PS nanospheres suspensions (Millipore Sigma, Canada) with a constant volume fraction ($\phi = 4\pi a^3 n/3$) at 8.37 × 10^{-9} or a constant number concentration at 4 × 10^6/mL were delivered into the microfluidic device by using a gastight syringe (Hamilton Laboratory Products, Reno, NV) and an Aladdin syringe pump (World Precision Instruments, Sarasota, FL). In the experimental investigation, we carried out plasmofluidic manipulation of nano-objects at four different flow speeds, namely, v_1 = 1.39 × 10^{-4} m/s (i.e., 0.1 mL/h), v_2 = 6.94 × 10^{-4} m/s (i.e., 0.5 mL/h), v_3 = 2.08 × 10^{-3} m/s (i.e., 1.5 mL/h), and v_4 = 6.94 × 10^{-3} m/s (i.e., 5 mL/h). This range of flow speeds was selected as it covers the typical flow conditions used in most biochemical analysis applications.[3,31,33] To analyze the plasmonic near-field trapping performance, four types of PS nanospheres with different diameters of 50, 100, 200, and 500 nm were studied individually. The bulk refractive index changes and unstable trappings could be eliminated by dynamic buffer flushing. The plasmonic CPSI spectra within the whole trapping process were recorded in real-time and the phase conditions were calculated based on the windowed Fourier transform (WFT) method.[18,34] Due to the localized plasmonic effect, the linear polarized transverse magnetic light showed significant transition in phase after total internal reflection on the metal−dielectric interface, and the phase transition only appeared at the LSPR resonance frequency.[18]

Preparation of Biological Nanovesicles. Exosomes were isolated using a previous published protocol. In brief, the conditioned

https://doi.org/10.1021/acsami.2c12651
ACS Appl. Mater. Interfaces 2022, 14, 47409−47419

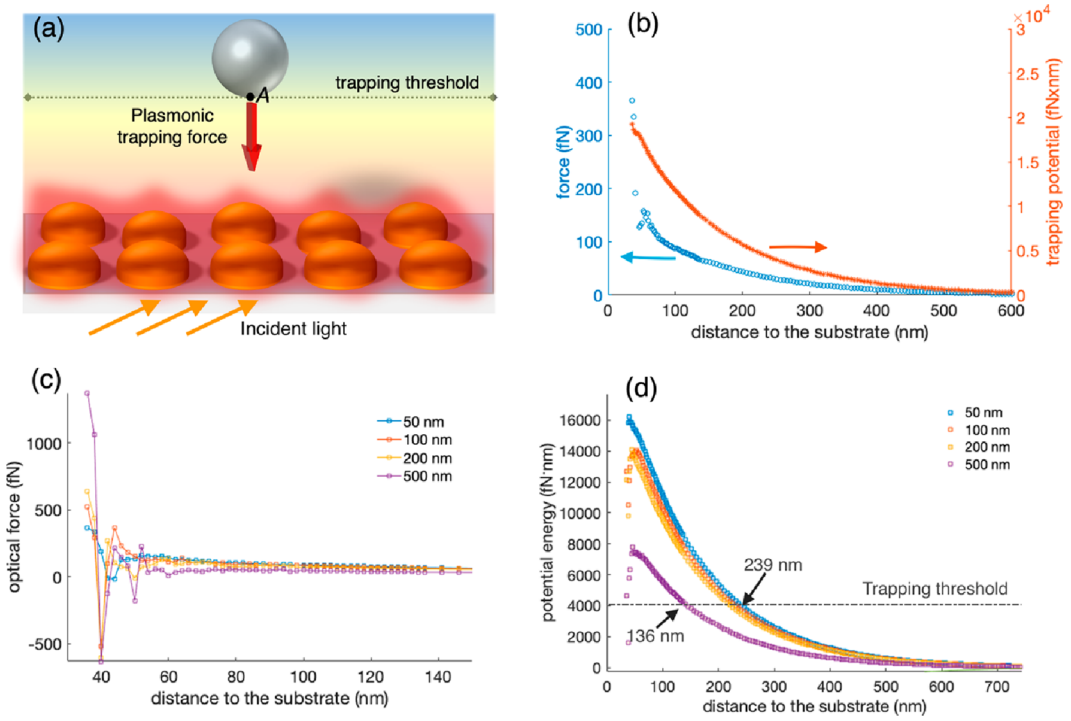

Figure 3. (a) schematic illustration of the optical trapping force near the plasmonic AuNI chip. The dash line indicated the trapping threshold based on the thermal energy. (b) The optical trapping force and the corresponding potential curve of 50 nm particles as a function of particle position along the y direction. (c) the optical near-field force of nano-objects with different diameters ranging from 50 to 500 nm. (d) The trapping potential of nano-objects along *y*-direction for nanospheres with different sizes. The zero distance to the substrate in (b), (c), and (d) referred to the reference surface of the glass substrate, while the minimum simulation results, starting from 36 nm, referred to the condition that the dielectric nano-objects were in direct contact with the protruding AuNI.

culture medium was centrifuged at 300 × g for 10 min. Then, the resultant supernatant was further centrifuged at 16 500 × *g* for 20 min followed by filtration of successive supernatant through 0.2 μm filter (to remove apoptotic bodies and microvesicles). The resultant supernatant was ultracentrifuged at 120 000 × *g* for 70 min to extract exosomes.

High- and low-density lipoprotein (HDL and LDL, with diameters of 10−30 nm) was isolated from the human plasma by KBr-density gradient ultracentrifugation approach. In brief, 500 μL of plasma was mixed with 1000 μL of 0.15 M NaCl/1 mM EDTA (d = 1.004) and 500 μL of 34.4% KBr (d = 1.2391), and the density was adjusted to 1.068 g/mL. The mixture was ultracentrifuged at 120 000 rpm for 6 h at 4 °C. Then, 200 μL of the bottom fraction of the ultracentrifuged sample was mixed with 900 μL of 46.5% KBr solution (d = 1.32), and the density of the solution was adjusted to 1.21 g/mL. Finally, the solution was centrifuged at 120 000 rpm for 16 h at 4 °C, and the upper fraction (15 mm from the bottom) was collected as the extracted lipoprotein.

RESULTS AND DISCUSSIONS

Evanescent Fields for Nanoscale Trapping. Evanescent wave optics are widely used in fiber optic and dielectric waveguide biosensors.[35] The excited near-fields extend to a short distance from the interface, which allow for real-time interrogation of binding events. SPP and LSPR also harnessed the photoinduced near-fields to sense the local changes at the glass−metal−analyte interface.[36] We first simulated the near-field distributions of these three configurations Figure 2a−d, so as to understand their feasibility for dynamic nanoparticle trapping and *in situ* sensing. In the numerical analysis of the evanescent wave with a glass−water interface, our three-dimensional (3D) model consisted of a 1000 nm glass layer with the refractive index of 1.515 (at 600 nm) and a 1200 nm water layer with the refractive index of 1.330 (at 600 nm), as shown in Figure 2a,b. In Figure 2e, the inclined incident angle was prescribed to 65° so that TIR occurred at the glass−water interface, and an evanescent wave with a maximum electric field intensity (E_z) appeared on the water side, linking the positively and negatively charged magnetic areas in an *xy*-plane. With the SPP configuration as shown in Figure 2c, the electron cloud was excited resonantly and the derived SPR electric field was apparently stronger than that on the glass−water interface. At the nominal incident angle of 81°, the maximum near-field intensity of the SPR evanescent wave on the water side was about ~2 × 10^4 V/m. The SPP excitation condition, however, was still a sensitive function of the incident angle and Au film thickness as illustrated in Figure 2f. Generally, the inserted gold nanofilm enhanced the near-field intensity and doubled the maximum field intensity relative to the evanescent wave on the glass/water interface.

Under the stimulation of p-polarized light, localized plasmonic field was generated in the direct vicinity of AuNIs. Figures 2d and S1a illustrated the photon-induced LSPR near-fields on the AuNIs substrate. For the plasmonic AuNI-chip fabricated by the thermal dewetting method, the nanoislands with a tunable diameter and interparticle gaps could be partly embedded into the glass substrate and exhibit good stability and durability. The excited near-field intensity associated with plasmonic phenomena also depend strongly on the nanoscale arrangement. In order to provide a comprehensive understanding of the AuNI near-field distribution, further detailed numerical analysis, investigating the impact of the particle diameter, embedded depth and interparticle gap of AuNI were discussed in Figure S1. Generally, based on the TM-AFM

https://doi.org/10.1021/acsami.2c12651
ACS Appl. Mater. Interfaces 2022, 14, 47409−47419

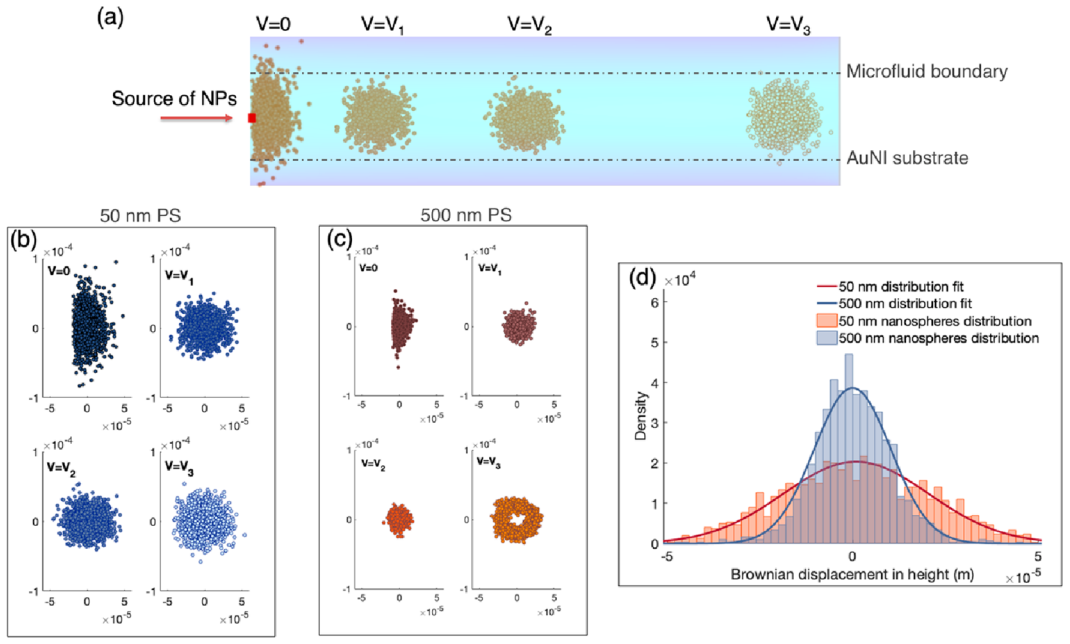

Figure 4. (a) Schematic illustration of the random distribution of nanospheres derived by Brownian motion. The red-dot in the center of microfluidics is the initial position and source of nanoparticles. The two dash-lines indicated the microfluidic boundary of top PDMS cover and AuNIs substrate, respectively. The nanoparticle distribution of (b) 50 nm particles and (c) 500 nm particles at t = 10 s with the different flow rates. The nonzero flow rates were $v_1 = 1.39 \times 10^{-4}$ m/s (i.e., 0.1 mL/h), $v_2 = 2.08 \times 10^{-3}$ m/s (i.e., 1.5 mL/h), and $v_3 = 6.94 \times 10^{-3}$ m/s (i.e., 5 mL/h). The O-shape distribution under v_3 represented an equilibrium condition induced by the shearing lift force and wall-lift force. (d) The distribution of y-displacements of nanoparticles demonstrated its dependence on the particle diameter. The induced flow rate is $v_1 = 1.39 \times 10^{-4}$ m/s and the time is 10 s.

results shown in Figure 1b, the synthetic AuNIs possessed a mean diameter of 40 nm with 6 nm embedment, and the interparticle gap was less than 10 nm. Based on this AuNIs configuration, the numerical analysis verified the amplified plasmonic fields and indicated that the maximum near-field intensity can be elevated to about 1.0×10^5 V/m (Figure S1d). Compared to the maximum near fields at the glass/water interface and SPP Au/water interface, LSPR generated by the AuNIs led to the highest near-field intensity and gradient as shown in Figures 2g and S2. In the following section, this configuration will be used as the standard model for evaluating the theoretical plasmonic trapping force and potential energy.

Trapping Force and Potential Energy of the LSPR Near-Field. When the nanoparticle approaches the near-field, the spatial field-gradient induces a trapping force as shown in Figure 3a. Based on the FEM plasmon-field simulation, the near-field trapping forces were subsequently calculated by using the Maxwell's stress tensor (MST).[37] It is worth noting that the forces are critically dependent upon the intrinsic characteristics (e.g., size, shape, and refractive index) of the trapped particles as well as the envelop external field (i.e., the plasmonic fields (Figure S2)). As the dielectric PS nanospheres were selected as the manipulating target in this plasmofluidic system, the polarization of the nano-objects and Lorentz force were not considered in this work. The averaged time-independent electromagnetic force F_p exerted on the particle can be calculated from the integration of the MST over the surface of the particle,[38] and is given as

$$F_p = \frac{1}{2} Re\left(\int \overline{\overline{T}} \cdot \vec{n} \, dS \right) \quad (1)$$

where $\vec{n}$ is a normal vector pointing away from the nano-object surface S, and $\overline{\overline{T}}$ is the time-independent MST.[13,39] We defined the surface point closest to the trapping interface as A (Figure 3a), and designated the tangent plane passing through A as the plane of nano-object. The trapping potential, $U(r)$, resulting from the optical forces determines the stability of the near-field trap, which can be obtained from

$$U(r) = \int_{\infty}^{r} F_p(r) \, dr \quad (2)$$

where r is the relative gap distance from the plane of nano-object to the glass substrate. To gain insights into the deflection mechanisms associated with plasmonic nanostructures, we first calculated the field distribution for a 50 nm PS nanoparticle, as illustrated by the dielectric nanosphere in Figure 3a. The highly localized plasmonic field (Figure S2) produced steep field gradients which generated a large gradient optical force and trapping potential, as illustrated in Figure 3b. The surface of the glass substrate (Figure S2) was defined as the reference zero-height plane. Considering the height of AuNI in the simulation, the minimum distance to the substrate (36 nm) as shown in Figure 3b–d referred to the protruding height of AuNI. Figure 3c provided the transverse trapping force along y-direction for nanospheres with different sizes. The trapping potentials near the AuNIs substrate were retrieved with eq 2 and given in Figure 3d. At room temperature of 300 K, the thermal energy of the nano-object $1K_BT$ (where K_B is Boltzmann constant) can be calculated to be 4.1×10^{-21} N·m (or $4.1 \times 10^3 f$N·nm). This thermal energy was utilized as the threshold value for evaluating the optical trapping: the trapping force produced by the plasmonic near-field should be sufficient to trap nano-objects against Brownian motion.[40] The offset distance as shown in Figure 3d is defined as the separation gap between the plane of nano-object and the glass substrate. It was found that the 50 nm nanospheres could

https://doi.org/10.1021/acsami.2c12651
ACS Appl. Mater. Interfaces 2022, 14, 47409−47419

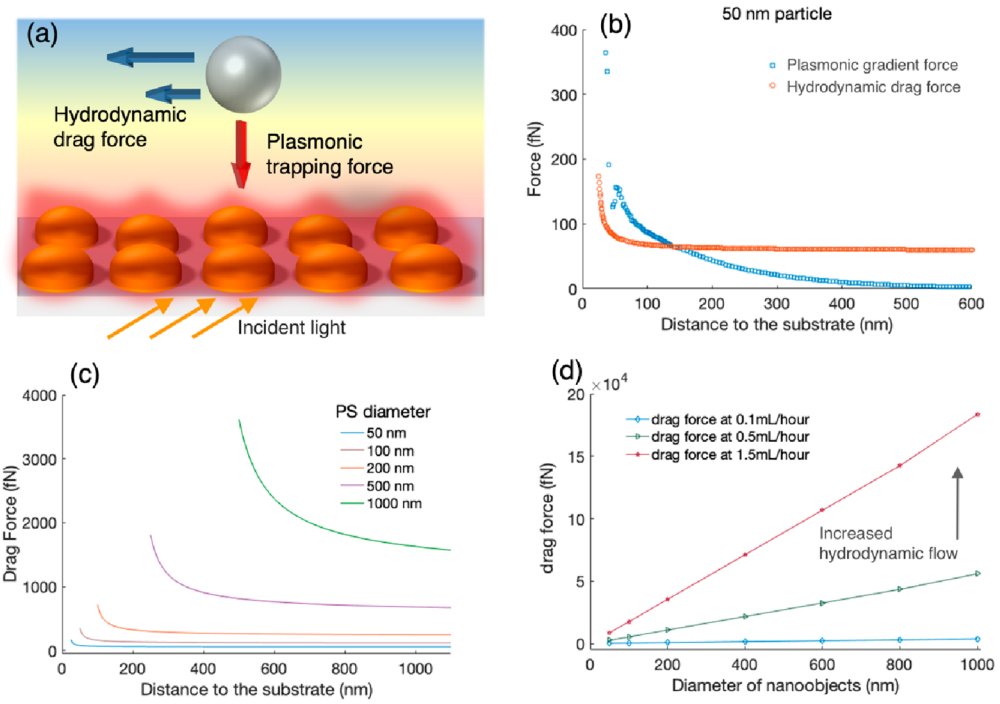

Figure 5. (a) schematic illustration of the hydrodynamic drag force and optical trapping force for nanoparticles near the plasmonic AuNI chip. (b) The optical trapping force and hydrodynamic drag force of 50 nm particles as a function of particle position at the constant flow rate of 0.1 mL/h. (c) The transverse components of the hydrodynamic force along *y*-direction for microparticles with different sizes at the flow rate of 0.1 mL/h. (d) The maximum hydrodynamic forces depending on the particle diameter with different flow rates.

be captured by the plasmonic near-field within an extended distance of 239 nm from the AuNI surface. This trapping volume decreased with the increasing diameter of the nanospheres as shown in Figure 3d. For instance, the height of the trapping volume decreased to only 136 nm for the 500 nm nanosphere as shown in Figure 3d. When the nanospheres cross the threshold, the trapping potential energy is larger than the thermal energy, therefore the plasmonic near-field trapping force becomes the dominant factor in the *y*-axis direction and pulling the nanospheres to the AuNI surface with even stronger gradient force.

Brownian Motion of Nanosphere in Microfluidics. At a position far away from the near-field AuNI substrate, two major factors act on suspended neutrally buoyant nano-objects and influence their spatial distribution (i.e., the Brownian motion and the hydrodynamic forces).[41] Understanding of Brownian motion and microfluidic induced forces of nanoparticles may offer precise spatiotemporal control over mass transport and facilitate the development of plasmofluidic trapping and optical biosensing. Herein, we initially studied the Brownian motion of the nano-objects along the *y*-axis direction. By using the dynamic light scattering (DLS) measurement (Figure S3a,b), we first obtained the actual size of different PS nanoparticles and used these as the input for Brownian motion simulation and the displacement calculation. Through the FEM simulation with COMSOL Multiphysics, the distribution of small nanoparticles (i.e., 50 nm PSL) and large nanoparticle (i.e., 500 nm PSL) were theoretically compared under different hydrodynamic flows. The initial position of the PS nanoparticles (with fixed number of 5×10^3) was fixed at the center of the channel (Figure 4a), which was used to simulate the source of the PS nanoparticle from the transport channel (with 0.1 mm width). The random distribution of 50 nm PS nanoparticles induced in four different flow velocity fields (i.e., 0, 1.39×10^{-4}, 2.08×10^{-3}, and 6.94×10^{-3} m/s) and a fixed time duration (i.e., 10 s) were schematic illustrated in Figure 4a. These nonzero flow rates (i.e., 1.39×10^{-4}, 2.08×10^{-3}, and 6.94×10^{-3} m/s) corresponded to three typical sensing flow rates of 0.1 mL/h, 1.5 mL/h and 5 mL/h used in our microfluidic biosensing system. In a static microfluidic channel (100 μm × 2000 μm) without flow, the thermal Brownian motion of 50 nm PS nanoparticles in the fluid causes the random collisions among the nano-objects and makes them spread out over time. In Figure 4b,c, we directly compared the size- and flow-dependent Brownian motions. Generally, the Brownian motion is more significant for small nano-objects. For instance, 50 nm PS nanoparticles demonstrated higher Brownian displacement than of 500 nm PS nanospheres in water. As shown in Figure 4a,b, the displacement of 50 nm nanoparticles covered a large aera within the microfluidic channel, which indicated the random Brownian motion could play an important role in driving the nanoparticles to reach the AuNI plasmonic-trapping interface. This random walking in the microfluidics could be one of the dominating far-field driving factors to facilitate the near-field tapping of 50 nm particles. With the same time and temperature condition, the Brownian displacement of 500 nm nanoparticles significantly reduced compared to 50 nm nanoparticles (Figure 4c). With nonzero flow rates in the microfluidics, the fully developed laminar flow confines the nanoparticles and reduces the maximum Brownian displacement. This effect is more significant for large-sized nanospheres (i.e., 500 nm as shown in Figure 4c), but has a limited impact on small-sized nanosphere (i.e., 50 nm as shown in Figure 4b). Therefore, in the microfluidic-based plasmonic trapping channel, smaller nanoparticles demonstrated a larger Brownian displacement within the channel (Figure 4d), so that the nanospheres could be trapped through the combined

https://doi.org/10.1021/acsami.2c12651
ACS Appl. Mater. Interfaces 2022, 14, 47409−47419

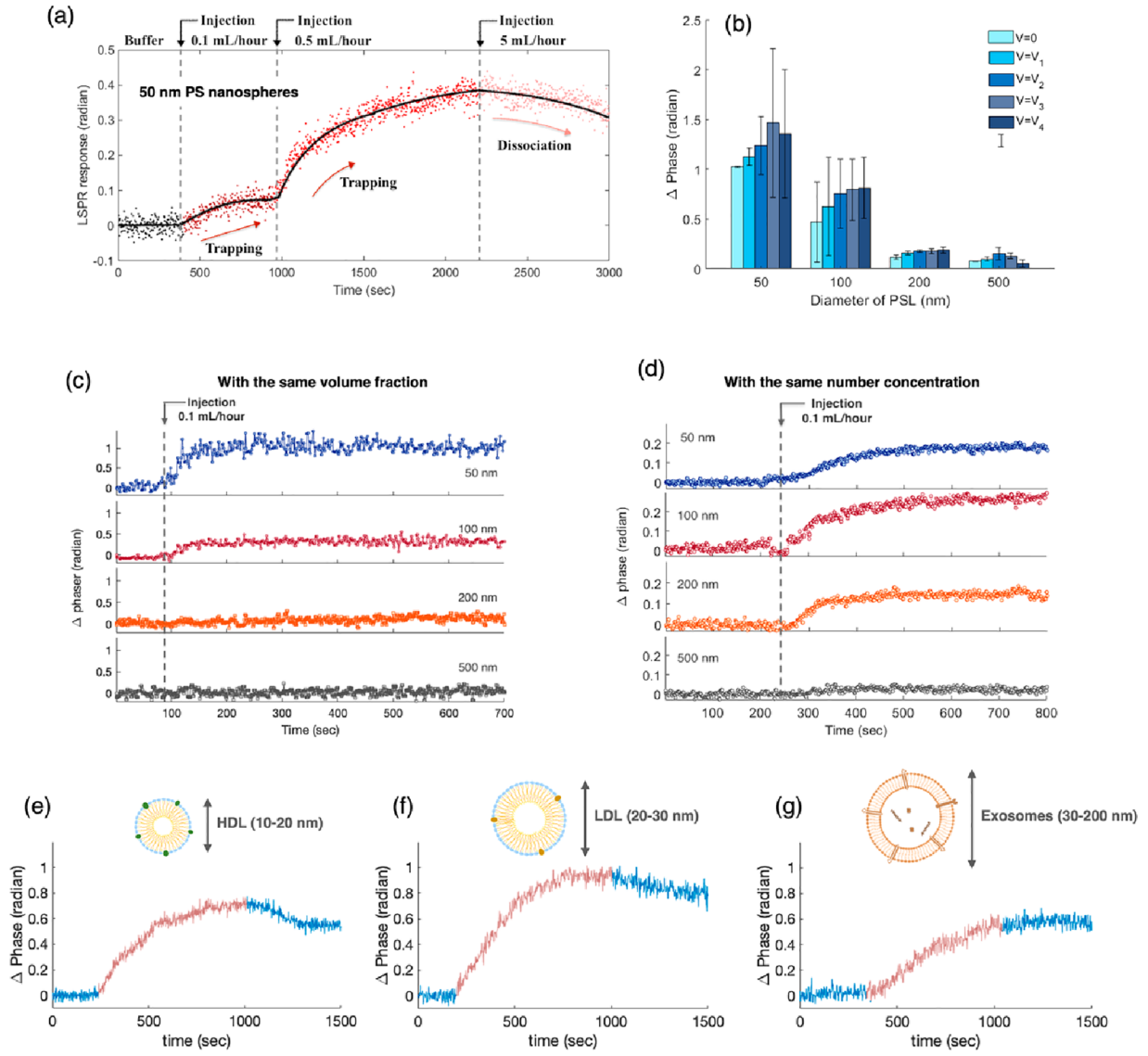

Figure 6. (a) Real-time dynamic LSPR responses for trapping 50 nm nanospheres at different flow rates. (b) LSPR responses of trapping nanospheres with different sizes and under different hydrodynamic flow speeds. $V_1 = 1.39 \times 10^{-4}$ m/s; $V_2 = 6.95 \times 10^{-4}$ m/s; $V_3 = 2.08 \times 10^{-3}$ m/s; and $V_4 = 6.95 \times 10^{-3}$ m/s. The volume fraction of different nanospheres is constant at $\phi = 8.37 \times 10^{-9}$. All phase sensitive LSPR experiments were repeated three times ($n = 3$) and the error bars for each PSL diameter and flow speed represented the error of three repeating tests. (c) Real-time trapping comparison of nanoparticles of different sizes (with the same volume fraction at 8.37×10^{-9}) at a constant flow rate of 0.1 mL/hour. (d) Real-time trapping comparison of nanoparticles with different sizes and same number concentration at 4×10^6 /ml. Real-time LSPR sensorgrams of plasmofluidic trapping of biological nanovesicles (e) HDL with typical diameter 10−20 nm, (f) LDL with typical diameter 20−30 nm, and (g) exosomes with diameter range 30−200 nm. The direct nanovesicle interaction region was highlighted in red, and the buffer rinse/flush was given in blue.

effects of random diffusion and the gradient plasmonic trapping force. Even at the highest flow rate in our study, nano-objects with small diameter, e.g., 50 nm, could still diffuse into the plasmonic field through Brownian motion and be deflected by the trapping force. Furthermore, the higher the flow rate (0 m/s$< v < 2.08 \times 10^{-3}$ m/s), the lower the Brownian displacement was found for larger nanospheres (e.g., 500 nm) as shown in Figure 4c. In contrast, the reduction of the Brownian displacement of small PS nanoparticles (50 nm) was not significant (Figure 4b). This flow-rate-dependent Brownian motion further diminished the probability of large nanoparticle being deflected or trapped in the near-field. At flow rates higher than 6.94×10^{-3} m/s, the wall-lift force and shear gradient lift force of the 500 nm nanoparticles balance with each other, resulting in the inertial equilibrium position and forming an O-shape profile in the flow as shown in Figure 4c.

Hydrodynamic Drag Force Applied on the Nanoparticles. Microfluidic flow can also exert hydrodynamic drag force on the nano-objects, enabling their actuation and transport. The hydrodynamic drag force exerted on the spherical nano-objects with very small Reynolds numbers in the viscous fluid can be described by Stokes law ($F_{hd} = 6\pi\mu av$). As shown in Figure S4, the flow velocity in the microfluidic channel is nonuniform, with a lower velocity close to the boundary of the channel and higher at the center of the channel. When the nano-objects are close to the AuNI substrate, the hydrodynamic drag forces F_{hd} are highly

https://doi.org/10.1021/acsami.2c12651
ACS Appl. Mater. Interfaces 2022, 14, 47409−47419

dependent on the distance between the particle and the substrate. Thus, the Faxen correction factor[42] was used here to predict the hydrodynamic force around the near field:

$$F_{hd} = 6\pi\mu a v \left[1 - \frac{9}{16}\frac{a}{h} + \frac{1}{8}\left(\frac{a}{h}\right)^3 - \frac{45}{256}\left(\frac{a}{h}\right)^4 - \frac{1}{16}\left(\frac{a}{h}\right)^5\right]^{-1} \quad (3)$$

where μ is the viscosity, v is the particle velocity, a is its radius, and h is the distance from the center of the particle to the substrate. As the nanoparticles approach the plasmonic trapping interface, they could be directly affected by the plasmonic near-field and the hydrodynamic flow fields (Figure 5a). For instance, when the nano-objects approach the AuNI interface, the significantly increased electromagnetic field produced a trapping force due to the gradient field distribution. In the process of nanoparticle trapping, the plasmonic gradient force should surpass the flow-induced net lift force (composed of the shear-gradient lift force, wall lift force, Saffman force and Magnus force) in the vertical direction. For the nanoparticles used in this work, the diameters (<500 nm) were significantly smaller than the channel hydraulic diameter (190 μm), so the flow induced net lift force can be considered negligible compared to the hydrodynamic drag force (Figure S4) in the vertical direction.[43,44] Therefore, as discussed previously, trapping criterion in the vertical direction is based on the plasmonic near-field gradient force and Brownian motion. In the horizontal direction, the periodic plasmonic near-fields generated by the AuNIs (Figure S2) exert a gradient force on the dielectric nano-object and potentially balance the hydrodynamic drag force. Since the plasmonic near-field in the horizontal direction shows a comparable or an even stronger gradient than that in the vertical directions (Figure S2), for nanoparticle with the similar size as AuNIs, the hydrodynamic drag force can be balanced by the plasmonic gradient force in the horizontal direction. As shown in Figure 5b, when the dielectric nano-object (50 nm) approached to the AuNI surface (<140 nm), the plasmonic gradient force can surpass the hydrodynamic drag force (exerted by 1.39×10^{-4} m/s fluid) in the horizontal direction and trap the nano-object.

For large dielectric particles, their bottom surface overlaps multiple electromagnetic field periods in the horizontal direction, thereby reducing the gradient trapping force.

In addition, the hydrodynamic force was highly dependent on the particle size (Figure 5c). Under the same flow velocity of 1.39×10^{-4} m/s, the maximum hydrodynamic drag force dramatically increased from 150 fN (50 nm PS) to 3500 fN (500 nm PS) in the vicinity of the AuNI surface. Therefore, the hydrodynamic force dominated the movement of these large nano-object and prevented them from being stably trapped. Moreover, by changing the flow rate (Figure 5d, i.e., 0.1 mL/h (1.39×10^{-4} m/s), 0.5 mL/h (6.95×10^{-4} m/s), 1.5 mL/h (2.08×10^{-3} m/s) and 5 mL/h (6.94×10^{-3} m/s)), the hydrodynamic drag force can be adjusted, so as to control the physical behavior of different nano-object in the vicinity of the AuNI surface.

Direct Trapping and Sensing of Dielectric Nano-Objects with the Plasmofluidic AuNI-Chips. To confirm the practical trapping capability with the AuNI-based plasmofluidic chip, tests with dielectric PS nanospheres and biological nanovesicles (i.e., HDL, LDL and exosomes) were executed. The spectral phase response was modulated with the CPSI system. By subtracting the initial phase reference, which was established at the beginning of the blank buffer rinse, we calculated the temporal phase difference for each second during the plasmofluidic trapping tests. The real-time interferometric phase response of trapping 50 nm PS nanospheres was given in Figure 6a, depicting the process in which the nanosphere samples were injected into the detection flow channel at different flow rates (i.e., 0.1 mL/hour (1.39×10^{-4} m/s), 0.5 mL/h (6.95×10^{-4} m/s), and 5 mL/h (6.95×10^{-3} m/s)). When the nanospheres were trapped by the plasmonic field, the local refractive index change produced a phase shift. For instance, the 50 nm PS nanospheres solutions injected at 0.1 and 0.5 mL/hour produced a differential LSPR phase shift by 0.08 and 0.31 rad, respectively (Figure 6a). In contrast, the nanospheres dissociated from the trapping field under a higher flow rate of 5 mL/hour.

To verify the size-dependent trapping behaviors, we used AuNI plasmofluidic chips to individually test PS nanospheres with different diameters and record the LSPR phase responses caused by the local in situ plasmofluidic trapping. In each test, the PS nanosphere solution with the same volume fraction ($\phi = 8.37 \times 10^{-9}$, Table S1) was flowed into the AuNI plasmofluidic chip at a designated flow rate for 300s, followed by the reinjection of water buffer to flush the interface. The AuNIs trapping responses toward different nanospheres at various flow rates were illustrated in Figure 6b. The statistical data on the phase-sensitive LSPR responses of trapping different dielectric nano-objects were calculated from the results of three replicate tests ($n = 3$). The temporal responses of the PS nanospheres with different nanoparticle sizes (i.e., 50, 100, 200, and 500 nm) were compared. At a constant flow rate of 0.1 mL/hour, the solution of 50 nm PS nanospheres exhibited a high LSPR phase response of 1.06 rad (Figure 6b,c), which indicated the plasmofluidic trapping and the increase of the local refractive index. In comparison, the 100 nm PS nanospheres with the same volume fraction reported a weak response at about 0.46 rad. When the nanoparticle diameter increased to 500 nm, no obvious phase responses were found as shown in Figure 6b,c. This can be explained by the decrease trapping potential energy (Figure 3d) and the increased flow-induced force (Figures 4 and 5c) for a nano-object larger than 500 nm. By gradually elevating the flow rate from 1.09×10^{-4} to 2.08×10^{-3} m/s, 50 and 100 nm neutral nanospheres demonstrated a reliable trapping behaviors and the responses slightly increased as more nano-objects were delivered to the plasmofluidic trapping surface by the flow. In general, smaller nanoparticles (<100 nm) are more likely to be captured by the plasmofluidic surface, and the in situ sensing system provided a reliable response for evaluating the size-dependent near-field trapping of dielectric nanoparticle when the volume fraction was constant. In the current microfluidic system (Figure 1a), high flow speeds demonstrate the ability to confine nano-objects to the center of the laminar flow and thus reduce the mass transfer efficiency as illustrated in Figure 4. Therefore, for a nanosphere sample with a fixed number concentration, a high flow rate will reduce the biosensing response caused by the localized plasmonic manipulation. Since LSPR is sensitive to the mass or refractive index change in the vicinity of the plasmonic nanoparticles, a higher phase response referred to a higher volume of PS nanospheres were trapped by the plasmonic near-field. Therefore, a stronger phase response indicated a higher trapping efficiency and vice

https://doi.org/10.1021/acsami.2c12651
ACS Appl. Mater. Interfaces 2022, 14, 47409−47419

versa. It is worth noting that the LSPR sensing region (or the penetration depth of the localized plasmonic near-field) cannot envelop the entire trapped nanosphere, especially for larger nano-objects. Therefore, the differential phase responses cannot be directly used to determine the number of tapped nano-objects and calculate the quantitative trapping efficiency. Furthermore, PS nano-objects solutions with the same number concentration (4×10^6/mL, Table S1) were also tested by using the plasmofluidic trapping platform. It was found that PS nano-objects smaller than 200 nm can produce positive in situ trapping responses as shown in Figure 6d, while there was still no obvious positive response for the large nanoparticles (500 nm PS nanospheres) even if the volume fraction has increased to 2.09×10^{-6}.

The size-dependent plasmofluidic trapping tests of standard dielectric PS nano-objects demonstrated a good agreement with our simulation. Herein, three different extracellular biological nanovesicles (i.e., HDL, LDL, and exosomes) were used to validate the proposed plasmofluidic-based near-field optical trapping and sensing system. HDL and LDL are two types of plasma lipoprotein nanoparticles in extracellular fluids, with a typical diameter range of 10−20 nm and 20−30 nm, respectively. These two nanovesicles transport hydrophobic molecules in blood play an important role in atherosclerosis.[45,46] In our near-field plasmofluidic trapping test, both HDL and LDL samples (10 000× dilution of isolated specimens, Figure S5) produced a strong phase response at the constant flow rate of 1.5 mL/h as shown in Figure 6e,f. After flushing the AuNI chips with buffer solution, a small portion of unstable trapped dielectric nanovesicles can be removed and the final differential phase signals were found to be 0.54 and 0.80 rad for HDL and LDL, respectively. Furthermore, the decrease of LSPR biosensing signal also proved that the trapped nanoparticles were not firmly anchored on the AuNI chips, as is the case for covalent immobilization in conventional biosensing systems. Trapping (i.e., the control of nano-object movement) was a dynamic process. Nano-objects enriched near the AuNI interface can cause alterations in the refractive index and plasmonic phase response. Meanwhile, a fraction of the nano-objects could also move slowly near the interface and eventually escape from the trapping zone of the plasmonic near-field. Exosomes are another type of extracellular nanovesicles produced by most of the eukaryotic cells, with a typical diameter range of 30−200 nm.[47] The direct plasmofluidic trapping and parallel sensing test of exosomes (10 000× dilution of purified specimens with mean diameter at 172 nm, Figure S6) as shown in Figure 6g also provided a positive phase signal and the equilibrium response after buffer flushing was found to be 0.59 rad. By adjusting the hydrodynamic flow rates, different extracellular vesicles (e.g., exosomes and microvesicles) can be distinguished with the AuNI chip.[3] In the flow speed tests (Figure S7) we also found that the exosome trapping efficiency decreased at elevated microfluidic flow rates (5 mL/h) when compared to lower flow rates (e.g., 1.5 mL/h). The real-time biosensing phase response decreased from 0.59 to 0.36 rad after sample injection. This low response was caused by reductions in mass transfer and trapping efficiency at the high flow rate. Additionally, the phase response further decreased to 0.08 rad during the buffer flushing process. These experimental results indicate that exosomes and other targeted biological nano-objects could be removed from the interface by tuning the hydrodynamic flow fields.

The experimental results of these biological nanovesicles proved the feasibility of our proposed in situ near-field plasmofluidic trapping and sensing system. First, under a suitable hydrodynamic flow condition, near-field plasmonics excited by low irradiation power exhibited the ability to trapping dielectric nano-objects (i.e., HDL, LDL, and exosomes) smaller than 200 nm and achieved in situ monitoring through the LSPR transduction. By reasonably optimizing the electric field distribution and intensity, as well as the direction and form of the hydrodynamic fluid, the LSPR-based plasmofluidic system can be potentially used for label-free large-scale manipulating and trapping of dielectric nanoparticles, including the fast dielectric biological nanovesicles fractionation and on-site optical characterization. The proposed AuNI-based plasmofluidic nano-object manipulating system is currently unable to distinguish nanoparticles of similar sizes, as the LSPR near-field transduces refractive index alterations in the vicinity of the nanoparticle. Additional in situ biosensing characterization and fingerprinting techniques, such as surface enhanced Raman spectroscopy, could be used for selective sorting and screening.

CONCLUSIONS

Based on our computational and experimental investigation, we predicted and practically achieved the size-selective (<200 nm) plasmonic trapping and transducing of dielectric nano-objects within the microfluidic environment based on the AuNI plasmofluidic chip. The dynamic forces of nanospheres, ranging from 50 to 500 nm, were numerically analyzed under different TIR near-field optics and flow-induced hydrodynamic fields based on the finite element simulation. Specifically, plasmonic near-fields produced by LSPR coupling effect of nanoislands demonstrated stronger field gradient and intensity than that of the SPR configuration and dielectric TIR configuration. When the dielectric nano-objects flow into the designed microfluidic system (a high aspect-ratio microfluidic with 2 mm width and 0.1 mm profile height), the gradient force generated by the LSPR near-field, the flow-induced force and Brownian motion were considered as the main factors for the plasmofluidic trapping. It was found that smaller nano-objects (50 nm) were more likely to be enveloped by the LSPR near field, thus producing a stronger gradient force and trapping potential. The flow-induced lift forces and hydrodynamic drag force of small nano-objects can be balanced by the plasmonic trapping force. In addition, the Brownian motion was considered as the main far-field driving factor to facilitate the nano-objects to reach the AuNI surface and be trapped by plasmonic near-fields. The plasmofluidic trapping of nano-objects were further verified with the optimized AuNIs chips and differential phase sensing system. Experimental results confirmed that the PS nanospheres with diameter of 50−200 nm can be trapped by the localized near-fields, and the LSPR phase sensing system can monitor the in situ manipulation process in a real-time manner. Additional tests with biological nanovesicles, including HDL (approximate 10−20 nm), LDL (20−30 nm), and exosomes (30−200 nm) further validated the concept of large-scale optical trapping and parallel dynamic sensing without using complex optics and molecular tether. Therefore, we believe that this plasmofluidic concept, which offered a nondestructive method for sensing and manipulating of various dielectric nano-objects, can be a potential bioanalytical approach for developing the new generation biosensor, which combining the capability of

https://doi.org/10.1021/acsami.2c12651
ACS Appl. Mater. Interfaces 2022, 14, 47409−47419

optical trapping, in situ manipulation, parallel nontether sensing, and on-site characterization.

■ ASSOCIATED CONTENT

Supporting Information

The Supporting Information is available free of charge at https://pubs.acs.org/doi/10.1021/acsami.2c12651.

Methodology of theoretical models, fabrication of AuNIs based plasmofluidic chip, AuNI electromagnetic filed distribution, optimization, DLS of PSL nanoparticles, flow velocity distribution, Western blot of HDL/LDL, exosomal size distribution, biosensing results of exosomes at different flow speed (PDF)

■ AUTHOR INFORMATION

Corresponding Authors

Jing Wang − *Institute for Environmental Engineering, ETH Zürich, CH-8093 Zürich, Switzerland; Laboratory for Advanced Analytical Technologies, Empa, Swiss Federal Laboratories for Materials Science and Technology, Dübendorf 8600, Switzerland;* orcid.org/0000-0003-2078-137X; Email: jing.wang@ifu.baug.ethz.ch

Andrew deMello − *Institute for Chemical and Bioengineering, Department of Chemistry and Applied Biosciences, ETH Zürich, CH-8093 Zürich, Switzerland;* Email: andrew.demello@chem.ethz.ch

Authors

Guangyu Qiu − *Institute for Environmental Engineering, ETH Zürich, CH-8093 Zürich, Switzerland; Laboratory for Advanced Analytical Technologies, Empa, Swiss Federal Laboratories for Materials Science and Technology, Dübendorf 8600, Switzerland; Institute of Medical Robotics, School of Biomedical Engineering, Shanghai Jiao Tong University, Shanghai 200240, China*

Ying Du − *Institute for Chemical and Bioengineering, Department of Chemistry and Applied Biosciences, ETH Zürich, CH-8093 Zürich, Switzerland; College of Science, Zhejiang University of Technology, Hangzhou 310023, China*

Yujia Guo − *College of Science, Zhejiang University of Technology, Hangzhou 310023, China*

Yingchao Meng − *Institute for Chemical and Bioengineering, Department of Chemistry and Applied Biosciences, ETH Zürich, CH-8093 Zürich, Switzerland;* orcid.org/0000-0001-9097-0868

Zhibo Gai − *Department of Clinical Pharmacology and Toxicology, University Hospital Zurich, University of Zürich, Zürich 8091, Switzerland*

Ming Zhang − *College of Science, Zhejiang University of Technology, Hangzhou 310023, China*

Complete contact information is available at: https://pubs.acs.org/10.1021/acsami.2c12651

Author Contributions

[▽]G.Q. and Y.D. contributed equally to this work. The manuscript was written through contributions of all authors. All authors have given approval to the final version of the manuscript.

Notes

The authors declare no competing financial interest.

■ ACKNOWLEDGMENTS

This project has received funding from the European Union's Horizon 2020 research and innovation programme under the Marie Sklodowska-Curie (MSC) grant agreement no. 791144. This work is also supported by the National Natural Science Foundation of China (grant no. 61705196).

■ REFERENCES

(1) Maragò, O. M.; Jones, P. H.; Gucciardi, P. G.; Volpe, G.; Ferrari, A. C. Optical Trapping and Manipulation of Nanostructures. *Nat. Nanotechnol.* **2013**, *8* (11), 807.

(2) Dobson, J. Remote Control of Cellular Behaviour with Magnetic Nanoparticles. *Nat. Nanotechnol.* **2008**, *3* (3), 139.

(3) Thakur, A.; Qiu, G. Y.; NG, S.-P.; Guan, J. T.; Yue, J. B.; Lee, Y. J.; Wu, C. M. L. Direct Detection of Two Different Tumor-Derived Extracellular Vesicles by SAM-AuNIs LSPR Biosensor. *Biosens. Bioelectron.* **2017**, *94*, 400−407.

(4) Oliveira, G. H.; Galante, M. T.; Martins, T. T.; dos Santos, L. F.; Ely, F.; Longo, C.; Gonçalves, R. V.; Muniz, S. R.; Nome, R. A. Real Time Single TiO2 Nanoparticle Monitoring of the Photodegradation of Methylene Blue. *Sol. Energy* **2019**, *190*, 239−245.

(5) Yang, A. H.; Moore, S. D.; Schmidt, B. S.; Klug, M.; Lipson, M.; Erickson, D. Optical Manipulation of Nanoparticles and Biomolecules in Sub-Wavelength Slot Waveguides. *Nature* **2009**, *457* (7225), 71−75.

(6) Huang, Y.; Ewalt, K. L.; Tirado, M.; Haigis, R.; Forster, A.; Ackley, D.; Heller, M. J.; O'Connel, J. P.; Krihak, M. Electric Manipulation of Bioparticles and Macromolecules on Microfabricated Electrodes. *Anal. Chem.* **2001**, *73* (7), 1549−1559.

(7) Snezhko, A.; Aranson, I. S. Magnetic manipulation of self-assembled colloidal asters. *Nat. Mater.* **2011**, *10* (9), 698−703.

(8) Sazan, H.; Piperno, S.; Layani, M.; Magdassi, S.; Shpaisman, H. Directed Assembly of Nanoparticles into Continuous Microstructures by Standing Surface Acoustic Waves. *J. Colloid Interface Sci.* **2019**, *536*, 701−709.

(9) Dholakia, K.; Reece, P.; Gu, M. Optical Micromanipulation. *Chem. Soc. Rev.* **2008**, *37* (1), 42−55.

(10) Bradac, C. Nanoscale Optical Trapping: a Review. *Advanced Optical Materials* **2018**, *6* (12), 1800005.

(11) Juan, M. L.; Righini, M.; Quidant, R. Plasmon Nano-Optical Tweezers. *Nat. Photonics* **2011**, *5* (6), 349.

(12) Berthelot, J.; Acimovic, S. S.; Juan, M. L.; Kreuzer, M. P.; Renger, J.; Quidant, R. Three-Dimensional Manipulation with Scanning Near-Field Optical Nanotweezers. *Nat. Nanotechnol.* **2014**, *9* (4), 295−299.

(13) Marchington, R. F.; Mazilu, M.; Kuriakose, S.; Garces-Chavez, V.; Reece, P. J.; Krauss, T. F.; Gu, M.; Dholakia, K. Optical deflection and sorting of microparticles in a near-field optical geometry. *Opt Express* **2008**, *16* (6), 3712−3726.

(14) Jiang, Y.; Narushima, T.; Okamoto, H. Nonlinear Optical Effects in Trapping Nanoparticles with Femtosecond Pulses. *Nat. Phys.* **2010**, *6* (12), 1005−1009.

(15) Gu, M.; Haumonte, J. B.; Micheau, Y.; Chon, J. W. M.; Gan, X. S. Laser Trapping and Manipulation Under Focused Evanescent Wave Illumination. *Appl. Phys. Lett.* **2004**, *84* (21), 4236−4238.

(16) Garces-Chavez, V.; Quidant, R.; Reece, P. J.; Badenes, G.; Torner, L.; Dholakia, K. Extended Organization of Colloidal Microparticles by Surface Plasmon Polariton Excitation. *Phys. Rev. B* **2006**, *73* (8), 085417.

(17) Righini, M.; Zelenina, A. S.; Girard, C.; Quidant, R. Parallel and Selective Trapping in a Patterned Plasmonic Landscape. *Nat. Phys.* **2007**, *3* (7), 477−480.

(18) Qiu, G. Y.; Ng, S. P.; Wu, C. M. L. Differential Phase-Detecting Localized Surface Plasmon Resonance Sensor with Self-Assembly Gold Nano-Islands. *Opt. Lett.* **2015**, *40* (9), 1924−1927.

(19) Halas, N. J.; Lal, S.; Chang, W.-S.; Link, S.; Nordlander, P. Plasmons in Strongly Coupled Metallic Nanostructures. *Chem. Rev.* **2011**, *111* (6), 3913−3961.

(20) Ren, Y.; Chen, Q.; He, M.; Zhang, X.; Qi, H.; Yan, Y. Plasmonic Optical Tweezers for Particle Manipulation: Principles, Methods, and Applications. *ACS Nano* **2021**, *15* (4), 6105−6128.
(21) Pang, Y.; Gordon, R. Optical Trapping of 12 nm Dielectric Spheres Using Double-Nanoholes in a Gold Film. *Nano Lett.* **2011**, *11* (9), 3763−3767.
(22) Han, X.; Truong, V. G.; Thomas, P. S.; Chormaic, S. N. Sequential Trapping of Single Nanoparticles Using a Gold Plasmonic Nanohole Array. *Photonics Res.* **2018**, *6* (10), 981−986.
(23) Tanaka, Y.; Sasaki, K. Optical Trapping Through the Localized Surface-Plasmon Resonance of Engineered Gold Nanoblock Pairs. *Opt Express* **2011**, *19* (18), 17462−17468.
(24) Wang, K.; Schonbrun, E.; Steinvurzel, P.; Crozier, K. B. Scannable Plasmonic Trapping Using a Gold Stripe. *Nano Lett.* **2010**, *10* (9), 3506−3511.
(25) Huang, L.; Maerkl, S. J.; Martin, O. J. F. Integration of Plasmonic Trapping in a Microfluidic Environment. *Opt Express* **2009**, *17* (8), 6018−6024.
(26) Yin, S.; He, F.; Green, N.; Fang, X. Nanoparticle Trapping and Routing on Plasmonic Nanorails in a Microfluidic Channel. *Opt Express* **2020**, *28* (2), 1357−1368.
(27) Kim, J. Joining Plasmonics with Microfluidics: from Convenience to Inevitability. *Lab Chip* **2012**, *12* (19), 3611−3623.
(28) Oh, S.-H.; Altug, H. Performance Metrics and Enabling Technologies for Nanoplasmonic Biosensors. *Nat. Commun.* **2018**, *9* (1), 5263.
(29) Koya, A. N.; Cunha, J.; Guo, T. L.; Toma, A.; Garoli, D.; Wang, T.; Juodkazis, S.; Cojoc, D.; Proietti Zaccaria, R. Novel Plasmonic Nanocavities for Optical Trapping-Assisted Biosensing Applications. *Advanced Optical Materials* **2020**, *8* (7), 1901481.
(30) Zijlstra, P.; Paulo, P. M. R.; Orrit, M. Optical Detection of Single Non-Absorbing Molecules Using the Surface Plasmon Resonance of a Gold Nanorod. *Nat. Nanotechnol.* **2012**, *7* (6), 379−382.
(31) Qiu, G. G.; Gai, Z. B.; Tao, Y. L.; Schmitt, J.; Kullak-Ublick, G. A.; Wang, J. Dual-Functional Plasmonic Photothermal Biosensors for Highly Accurate Severe Acute Respiratory Syndrome Coronavirus 2 Detection. *ACS Nano* **2020**, *14* (5), 5268−5277.
(32) Qiu, G. Y.; Ng, S. P.; Wu, C. M. L. Bimetallic Au-Ag Alloy Nanoislands for Highly Sensitive Localized Durface Plasmon Resonance Biosensing. *Sensors and Actuators B-Chemical* **2018**, *265*, 459−467.
(33) Qiu, G.; Gai, Z.; Saleh, L.; Tang, J.; Gui, T.; Kullak-Ublick, G. A.; Wang, J. Thermoplasmonic-Assisted Cyclic Cleavage Amplification for Self-Validating Plasmonic Detection of SARS-CoV-2. *ACS Nano* **2021**, *15* (4), 7536−7546.
(34) Ng, S. P.; Wu, C. M. L.; Wu, S. Y.; Ho, H. P. White-Light Spectral Interferometry for Surface Plasmon Resonance Sensing Applications. *Opt. Express* **2011**, *19* (5), 4521−4527.
(35) Jensen, J. B.; Pedersen, L. H.; Hoiby, P. E.; Nielsen, L. B.; Hansen, T. P.; Folkenberg, J. R.; Riishede, J.; Noordegraaf, D.; Nielsen, K.; Carlsen, A.; Bjarklev, A. Photonic Crystal Fiber Based Evanescent-Wave Sensor for Detection of Biomolecules in Aqueous Solutions. *Opt. Lett.* **2004**, *29* (17), 1974−1976.
(36) Brolo, A. G. Plasmonics for Future Biosensors. *Nat. Photonics* **2012**, *6* (11), 709−713.
(37) Kim, J.; Martin, O. J. Studying the Different Coupling Regimes for a Plasmonic Particle in a Plasmonic Trap. *Opt. Express* **2019**, *27* (26), 38670−38682.
(38) Saleh, A. A. E.; Dionne, J. A. Toward Efficient Optical Trapping of Sub-10-nm Particles with Coaxial Plasmonic Apertures. *Nano Lett.* **2012**, *12* (11), 5581−5586.
(39) Almaas, E.; Brevik, I. Radiation Forces on a Micrometer-Sized Sphere in an Evanescent Field. *JOSA B* **1995**, *12* (12), 2429−2438.
(40) Yang, A. H.; Lerdsuchatawanich, T.; Erickson, D. Forces and Transport Velocities for a Particle in a Slot Waveguide. *Nano Lett.* **2009**, *9* (3), 1182−1188.
(41) Frank, M.; Anderson, D.; Weeks, E. R.; Morris, J. F. Particle Migration in Pressure-Driven Flow of a Brownian Suspension. *J. Fluid Mech.* **2003**, *493* (493), 363−378.
(42) Goldman, A. J.; Cox, R. G.; Brenner, H. Slow Viscous Motion Of a Sphere Parallel To a Plane Wall. I. Motion Through a Quiescent Fluid. *Chem. Eng. Sci.* **1967**, *22* (4), 637.
(43) Zhang, A.; Murch, W. L.; Einarsson, J.; Shaqfeh, E. S. Lift and Drag Force on a Spherical Particle in a Viscoelastic Shear Flow. *J. Non-Newtonian Fluid Mech.* **2020**, *280*, 104279.
(44) Di Carlo, D.; Irimia, D.; Tompkins, R. G.; Toner, M. Continuous Inertial Focusing, Ordering, and Separation of Particles in Microchannels. *Proc. Natl. Acad. Sci. U. S. A.* **2007**, *104* (48), 18892−18897.
(45) Navab, M.; Reddy, S. T.; Van Lenten, B. J.; Fogelman, A. M. HDL and Cardiovascular Disease: Atherogenic and Atheroprotective Mechanisms. *Nature Reviews Cardiology* **2011**, *8* (4), 222−232.
(46) Arsenault, B. J.; Boekholdt, S. M.; Kastelein, J. J. Lipid Parameters for Measuring Risk of Cardiovascular Disease. *Nature Reviews Cardiology* **2011**, *8* (4), 197−206.
(47) Van Niel, G.; d'Angelo, G.; Raposo, G. Shedding Light on the Cell Biology of Extracellular Vesicles. *Nat. Rev. Mol. Cell Biol.* **2018**, *19* (4), 213−228.

https://doi.org/10.1021/acsami.2c12651
ACS Appl. Mater. Interfaces 2022, 14, 47409−47419